Oxide Acidity Modulates Structural Transformations in Hydrogen Titanates during Electrochemical Li-Ion Insertion

Saeed Saeed, Simon Fleischmann, Takeshi Kobayashi, Zenonas Jusys, Eugene Mamontov, Naresh C. Osti, Noah P. Holzapfel, Haohong Song, Tao Wang, Sheng Dai, De-en Jiang, and Veronica Augustyn*

ABSTRACT: Hydrogen titanates (HTOs) form a diverse group of metastable, layered titanium oxides with an interlayer containing both water molecules and structural protons. We investigated how the chemistry of this interlayer environment influenced electrochemical Li^+-insertion in a series of HTOs, $H_2Ti_yO_{2y+1}{\cdot}nH_2O$ (y = 3, 4, and 5). We correlated the electrochemical response with the physical and chemical properties of HTOs using operando X-ray diffraction, in situ differential electrochemical mass spectroscopy, solid-state proton nuclear magnetic resonance, and quasi-elastic neutron scattering. We found that the potential for the first reduction reaction trended with the relative acidity of the structural protons. This mechanism was supported with first-principles density functional theory (DFT) calculations. We propose that the electrochemical reaction involves reduction of the structural protons to yield hydrogen gas and formation of a lithiated hydrogen titanate ($H_{2-x}Li_xTi_yO_{2y+1}$). The hydrogen gas is confined within the HTO lattice until the titanate structure expands upon subsequent oxidation. Our work has implications for the electrochemical behavior of insertion hosts containing hydrogen and structural water molecules, where hydrogen evolution is expected at potentials below the hydrogen reduction potential and in the absence of electrolyte proton donors. This behavior is an example of electrochemical electron transfer to a nonmetal element in a metal oxide host, in analogy to anion redox.

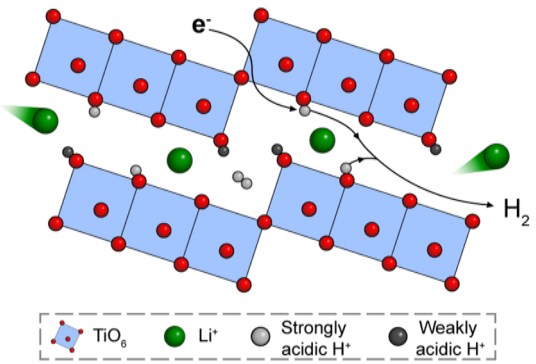

INTRODUCTION

Electrochemical energy storage technologies profoundly impact the global energy landscape and are now integral components of daily life for most humans. The critical role of rechargeable batteries in sustainable energy and increased global demand for portable power sources continues to stimulate research efforts into new materials and chemistries. Layered transition metal oxides are among the most important electrode materials for electrochemical energy storage. This is due to their ability to undergo electrochemical cation-insertion coupled electron transfer reactions to store charge. Titanium oxide-based materials are promising for energy storage and conversion applications due to their high natural abundance, low toxicity, and chemical tunability. Metastable transition metal oxides obtained via soft chemistry routes like ion exchange help to diversify the landscape of transition metal oxides for energy storage. By nature of the low temperature processing routes, these oxides can exhibit complex interlayer environments containing protons and structural water molecules. The solid-state electrochemical reactions of such materials in nonaqueous electrolytes are poorly understood, particularly the role of the interlayer protons and water molecules.[1−3] These have been hypothesized to facilitate electrochemical insertion reactions by providing fast solid-state transport pathways, perhaps involving a Grotthuss-type mechanism. HTOs prepared from proton exchange of alkali titanates exhibit electrochemical alkali cation insertion from nonaqueous electrolytes. For example, $H_2Ti_3O_7$, $H_2Ti_4O_9{\cdot}H_2O$, and $H_2Ti_6O_{13}$ undergo electrochemical reduction associated with the insertion of Li^+ near 1.5 V vs Li/Li^+.[4−8] All HTOs exhibit low first cycle Coulombic efficiency associated with irreversible processes, attributed to either H^+/Li^+ exchange or the reduction of H^+ to H_2. However, the electrochemical mechanisms involved during electrochemical cation insertion into the protonated interlayer remains an underdeveloped research area. In the case of HTOs, prior work by our group in aqueous acidic electrolytes showed that higher degrees of structural protonation resulted in larger proton insertion capacities.[9] Similarly, Kang et al. found that trititanate

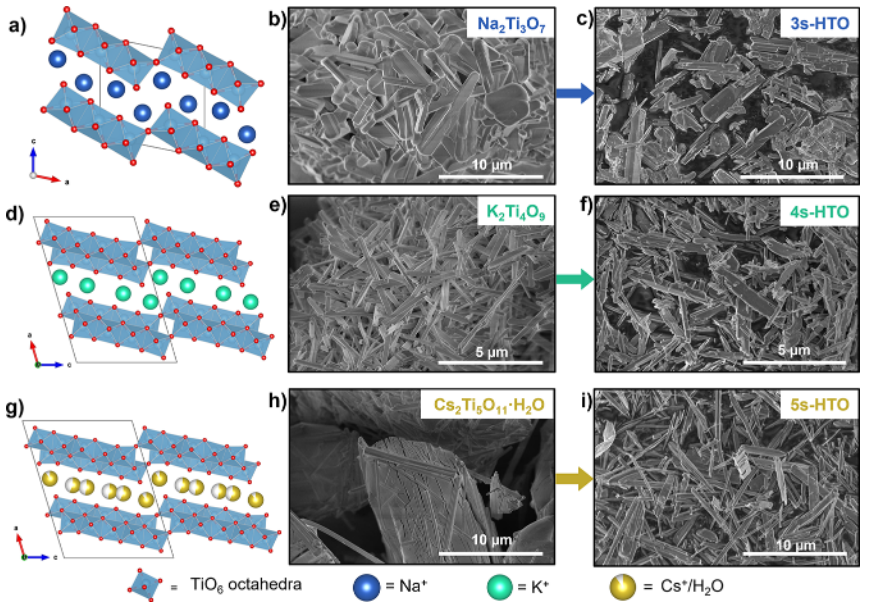

Figure 1. Crystal structures of the HTO precursors $Na_2Ti_3O_7$ (a), $K_2Ti_4O_9$ (d), and $Cs_2Ti_5O_{11}·H_2O$ (g). SEM images of HTO precursors $Na_2Ti_3O_7$ (b), $K_2Ti_4O_9$ (e), $Cs_2Ti_5O_{11}$ (h), and $H_2Ti_3O_7$ (3s-HTO) (c), $H_2Ti_4O_9·1.9H_2O$ (4s-HTO) (f), and $H_2Ti_5O_{11}·3H_2O$ (5s-HTO) (i).

structures with interlayer water and hydronium ions exhibit high proton conductivity, which favors fast electrochemical proton insertion.[10] We also found that HTOs undergo a dissolution degradation mechanism in aqueous electrolytes due to the formation of water-soluble Ti^{3+} at high states of charge.[11] As with other hydrous and protonated transition metal oxides that exhibit both an inner and outer electrochemical surface area, we expect the insertion electrochemistry of HTOs to be sensitive to the interlayer environment (e.g., degree of interlayer hydration, protonation) and the electrolyte (e.g., aqueous vs nonaqueous, pH, organic vs inorganic). This motivated us to study the solid-state electrochemistry of HTOs in nonaqueous electrolytes, where the absence of water molecules and protons in the electrolyte could lead to significantly different reactivity than in aqueous electrolytes. Our study has implications beyond HTOs, since many materials containing structural water molecules are primarily investigated in nonaqueous electrolytes due to the technological importance of achieving a high voltage rechargeable energy storage device.

Here, we investigate Li^+ insertion from a nonaqueous electrolyte in three hydrogen titanates (HTO; $H_2Ti_yO_{2y+1}$, y = 3, 4, 5) synthesized via selective acid etching of the alkali titanate precursors $Na_2Ti_3O_7$, $K_2Ti_4O_9$, and $Cs_2Ti_5O_{11}·H_2O$, respectively (Figure 1a,d,g). We utilize a combination of structural, analytical, and electrochemical techniques to understand the relationships between the relative activity of structural protons across this series of layered HTOs and the electrochemical Li^+ insertion mechanism. We use operando electrochemical X-ray diffraction (XRD), in situ differential electrochemical mass spectrometry (DEMS), ex situ solid-state ^1H and ^7Li solid-state (SS) nuclear magnetic resonance (NMR) spectroscopy, and acid−base titrations to probe the structural changes and gas evolution during electrochemical cycling and identify trends in structural proton pK_a. We show that structural protons are necessary for high Li^+ insertion capacity, while the acidity of these protons determines the onset potential for Li^+ insertion. Furthermore, we found that HTOs undergo irreversible structural changes associated with the reduction of the interlayer structural protons and hydrogen evolution. Upon oxidation, expansion of the interlayer spacing during oxidation from operando XRD perfectly matches the independently measured hydrogen release. Ex situ ^1H SSNMR confirms the disappearance of structural proton signals after extended electrochemical cycling, consistent with this structural change attributed to the loss of bulk structural protons.

EXPERIMENTAL METHODS

Materials Synthesis. Hydrogen titanates were synthesized using a previously reported solid-state synthesis method, followed by a topotactic proton-exchange reaction.[9,12−14] $H_2Ti_3O_7$ was prepared via acid exchange of $Na_2Ti_3O_7$, which was synthesized with a solid-state reaction. 10.0 g of Na_2CO_3 (anhydrous, Sigma-Aldrich) was dissolved in 150 mL of deionized (DI) water, followed by the addition of 22.0 g of TiO_2 (Aeroxide P25, Sigma-Aldrich). The mixture was stirred in air at 70 °C until all water evaporated to ensure homogenization. The remaining solid was ground with an agate mortar and pestle for 15 min. The solid powder was then transferred to an alumina crucible and heated in a box furnace to 800 °C for 20 h in air with a heating rate of 5 °C min^{-1}. The furnace was allowed to cool naturally, and the final product was collected and determined to be $Na_2Ti_3O_7$ via X-ray diffraction. $H_2Ti_3O_7$ powder was prepared by magnetic stirring of the as-synthesized $Na_2Ti_3O_7$ in 250 mL of 2.0 M HCl (Fisher Scientific) in an Erlenmeyer flask at 80 °C for 3 days in an oil bath. The flask was capped with a rubber stopper to prevent evaporation of the solution. The product was collected, rinsed with DI water, and centrifuged at 4500 rpm until the supernatant reached a pH value of ca. 5. The washed powder was then dried in air at 80 °C overnight.

$H_2Ti_4O_9·nH_2O$ was prepared using a similar method, starting with the solid-state synthesis of $K_2Ti_4O_9$ involving a 1:4 molar ratio of K_2CO_3 (anhydrous, Sigma-Aldrich) and nanostructured TiO_2. $H_2Ti_4O_9·nH_2O$ was prepared using the same acid stirring procedure described above. The product was collected, rinsed with DI water, and centrifuged at 4500 rpm with DI water until the supernatant reached a pH value of ca. 5. The powder was then dried in air at room temperature overnight. Further drying of the product at 80 °C dehydrates the powder, producing $H_2Ti_8O_{17}$.

$H_2Ti_5O_{11}·nH_2O$ was prepared from acid exchange of $Cs_2Ti_5O_{11}$, which was obtained from a solid-state reaction involving a 1:5 molar ratio of Cs_2CO_3 (anhydrous, Sigma-Aldrich) and nanostructured TiO_2. These precursors were dissolved in a beaker of 150 mL of DI

water and magnetically stirred at 50 °C until all water evaporated to ensure homogenization. The powder was then ground up in a mortar and pestle, transferred to an alumina crucible, and heated in a box furnace at 850 °C for 16 h with a heating rate of 5 °C min^{-1}. The furnace was allowed to cool naturally, and the resulting powder was reground and heated again to 950 °C for 16 h at a rate of 5 °C min^{-1} to obtain $Cs_2Ti_5O_{11}$. $H_2Ti_5O_{11}{\cdot}nH_2O$ was prepared by stirring the as-synthesized $Cs_2Ti_5O_{11}$ in 250 mL of 2.0 M HCl (Fisher Scientific) in an Erlenmeyer flask at 50 °C for 7 days in an oil bath. The product was collected, washed, and centrifuged at 4500 rpm with DI water until the supernatant reached a pH value of ca. 5. The powder was then dried in air at room temperature overnight.

Materials Characterization. Structural characterization was performed on the pristine HTO powders after drying at 80 °C overnight in air for $H_2Ti_3O_7$, and at room temperature overnight in air for $H_2Ti_4O_9{\cdot}nH_2O$ and $H_2Ti_5O_{11}{\cdot}nH_2O$. XRD data was collected on a PANalytical Empyrean diffractometer in Bragg–Brentano geometry equipped with a Cu–Kα radiation source. In situ heating XRD was taken with a PANalytical Empyrean diffractometer equipped with an HTK-1200N heating stage (Anton Paar) under a nitrogen atmosphere at a heating rate of 3 °C min^{-1} to 350 °C with scans collected using a 0.039°2θ step size and a scan step time of 26.01 s. SEM was performed on an FEI Verios 460L microscope. Raman spectroscopy measurements were performed using a WITec Alpha 300 Confocal Raman Spectroscopy Microscope (WITec Instruments Corp, Ulm, Germany) equipped with a 532 nm Nd:YAG laser, and an 1800 grooves cm^{-1} grating. Thermogravimetric analysis (TGA) was conducted using a Seiko Exstar TG/DTA6200 in air with a ramp rate of 5 °C min^{-1}. The surface area was measured by applying Brunauer–Emmett–Teller (BET) analyses to N_2 adsorption isotherms. N_2 adsorption–desorption experiments (Figure S1) were performed on a Tristar Micromeritics Setup at 77 K. All samples were degassed at 373 K under a N_2 flow overnight. Fourier transform infrared (FTIR) spectroscopy was collected on an Agilent Cary 630 spectrometer equipped with a diamond crystal attenuated total reflectance (ATR) stage in a transmission measurement configuration on powder samples. Spectra were collected from 650 to 4000 cm^{-1}.

Diffuse reflectance spectroscopy (DRS) data were collected on a Shimadzu UV–vis–NIR spectrophotometer (UV-3600) equipped with a Deuterium-Halogen lamp and an integrating sphere detector with a wavelength range of 200–1100 nm. A flat $BaSO_4$ (Alfa Aesar, 99%) surface served as the background reference. The analyte was evenly spread and then pressed onto the background reference. The reflectance of the analyte was recorded and then transformed using the Kubelka–Munk remission function.

Electrode Preparation. Electrodes were prepared by casting a slurry onto a conductive substrate, either stainless steel mesh or carbon paper. The slurries consisted of 80 wt % of active material (HTO), 10 wt % of polyvinylidene fluoride (PVDF, Arkema Kynar KV 900), and 10 wt % of carbon black (acetylene, 75 m^2 g^{-1}, Alfa Aesar) in *N*-methyl-2-pyrrolidone (NMP, Sigma-Aldrich). PVDF was first added to NMP and mixed until it dissolved. Carbon black and HTO were then added to the mixture and homogenized using a Thinky Mixer (AR-100, Thinky USA, Inc.). 1.5 mL of NMP was used for every 160 mg of HTO active material. Slurries were cast onto either stainless steel mesh (McMaster-Carr) or carbon paper (Fuel Cell Earth) by adding ~7 μL of slurry onto a 1 cm^2 electrode area using a micropipette, leading to a total mass loading of ~0.8 mg cm^{-2}. All electrodes were dried in air at 60 °C overnight unless otherwise stated.

Electrochemical Characterization. Electrochemical measurements were performed in a three-electrode cell using a 50 mL glass three-neck round-bottom flask (Sigma-Aldrich), with the HTO as the working electrode and Li metal (99.9% trace metals, Sigma-Aldrich) as the counter electrode and reference electrodes. All electrochemical measurements were carried out in an argon-filled MBraun Labstar Pro glovebox using a Bio-Logic VMP-3 potentiostat. The electrolyte was 1.0 M $LiClO_4$ (battery-grade, Sigma-Aldrich) in propylene carbonate (anhydrous, Sigma-Aldrich). Cyclic voltammetry was performed between 1.0–3.0 V vs Li/Li^+ at a scan rate of 0.2 mV s^{-1}. To determine the role of electrolyte cation on the electrochemical response of the HTOs, the HTO electrodes were cycled in a nonaqueous electrolyte containing a bulky cation, 0.1 M tetrabutylammonium perchlorate (Sigma-Aldrich) in propylene carbonate with a silver (Ag) wire (Alfa Aesar) as a pseudoreference electrode and a Pt wire (99.997%, Alfa Aesar) as the counter electrode.

Operando and Ex Situ Electrochemical X-Ray Diffraction. Synchrotron XRD was conducted at the Stanford Synchrotron Radiation Lightsource (SSRL) using beamline 2–1 in Bragg–Brentano geometry with an incident energy of 17 keV. A Pilatus 100 K area detector was used to collect the area diffraction patterns. The 2D diffraction patterns were compiled and integrated using a Python script developed at SSRL beamline 2–1.

Slurry-cast electrodes were used for operando XRD measurements. Slurries comprised of 80 wt % active material (HTO), 10 wt % polyvinylidene fluoride (PVDF, Arkema Kynar KV 900), and 10 wt % carbon black (acetylene, 75 m^2 g^{-1}, Alfa Aesar) in *N*-methyl-2-pyrrolidone (NMP, Sigma-Aldrich) 0.75 mL of NMP was used for every 80.0 mg of active material and the mixture was homogenized using a Thinky Mixer. 20–30 μL cm^{-2} of the slurry is cast onto stainless steel mesh and carbon paper substrates onto a 1.0 cm^2 geometric area. The masses of the electrodes are displayed in Table S1. The electrodes were then dried in an oven at 80 °C overnight.

Electrochemical measurements were performed in an in situ cell (Figure S2). The cell was composed of a 5.0 mm thick PEEK electrode holder with a 1/32″ thick fluorosilicone rubber gasket (McMaster-Carr) for preventing electrolyte leaks and a polyimide (Kapton) film to provide a low background window suitable for X-ray transmission. The in situ cell was assembled in an Ar-filled glovebox and transferred out, where it was then placed in a sealed helium (He) chamber. The full assembly was mounted onto the diffractometer. He gas was flowed through the chamber throughout the experiment. Cyclic voltammetry was performed in the in situ cell at a scan rate of 0.2 mV s^{-1} using a BioLogic SP150 potentiostat in a two-electrode configuration, with Li metal serving as the counter and reference electrode and 1.0 M $LiClO_4$ in propylene carbonate (PC) as the electrolyte. 2D diffraction patterns were collected with a fixed incident angle (θ) of 2° and a data acquisition time of 1–2 s. Full details of the experimental parameters used for each electrode are shown in Table S1.

Solid-State NMR Spectroscopy. The ^1H and ^7Li SSNMR experiments were conducted at 14.1 T on a Bruker Avance NEO spectrometer, equipped with a 2.5 mm magic-angle spinning (MAS) probe. The samples were packed in MAS zirconia rotors in a glovebox under an argon atmosphere. They were spun at 25 kHz using dry nitrogen to minimize the possibility of oxygen and moisture contamination.

Neutron Scattering. Quasielastic neutron scattering (QENS) experiments were performed at the Spallation Neutron Source of Oak Ridge National Laboratory using the backscattering silicon spectrometer (BASIS)[15] on the hydrated and dehydrated $H_2Ti_4O_9{\cdot}nH_2O$ and $H_2Ti_5O_{11}{\cdot}nH_2O$ ~ 7 g of each sample was evenly distributed in an aluminum foil, rolled into a pouch of roughly 1 mm in thickness, and loaded into a cylindrical aluminum container. The hydrated samples were prepared using the above-mentioned synthesis, dried overnight in the air at 65 °C, and immediately loaded into the containers and sealed using indium. The dehydrated samples were prepared by drying the as-synthesized powders at 140 °C overnight in air, then immediately transferred to the aluminum containers and sealed. An elastic intensity scan of each sample on heating at 1 K min^{-1} rate was also performed from 20 to 320 K. QENS spectra at 20 K (for instrument resolution), 333, 353, and 373 K were collected. QENS from an empty can with the same aluminum foil weight was also measured and used as a background. All QENS experiments were performed by running the instrument at the standard configuration (chopper frequency of 60 Hz, wavelength of the incident neutron bandwidth centered at 6.4 Å). This configuration provides an energy transfer range of ±100 μeV and a Q (momentum transfer vector) range of 0.2–2.0 $Å^{-1}$ with an energy resolution of 3.6 μeV (Q-averaged full width at half-maximum). Data were reduced and

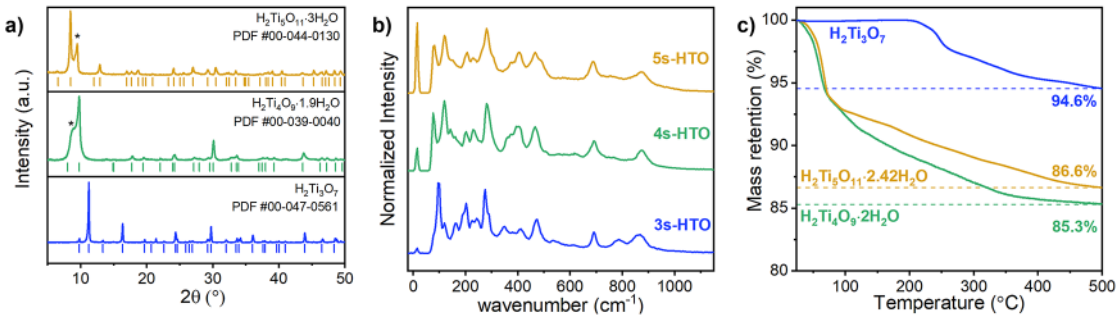

Figure 2. X-ray diffraction (a), Raman spectra (b), and thermogravimetric analysis (c) of 3s-HTO (blue), 4s-HTO (green), and 5s-HTO (yellow). * Indicates a secondary hydrated phase.

analyzed using Mantid and ICEMAN/QClimax software packages.[16,17]

Computational Methods. DFT calculations were performed using the Vienna ab initio Simulation Package (VASP)[18,19] with the Perdew–Burke–Ernzerhof (PBE)[20] form of the generalized-gradient-approximation exchange correlation functional. The projector augmented wave (PAW) potential was used to describe the electron–nuclei interaction.[21] An energy cutoff of 500 eV was used for the plane wave basis sets. The structure of $H_2Ti_3O_7$ used for calculations was based on a previously reported model,[9] while the structure of $Li_2Ti_3O_7$ was from Rousse et al. based on Rietveld refinement of synchrotron X-ray diffraction data.[22] The structures of $H_xLi_{2-x}Ti_3O_7$ were simulated by supercells containing 4-formula units. All degrees of freedom were relaxed with a force convergence criterion of 0.02 eV $Å^{-1}$ and an energy convergence criterion of 10^{-5} eV. A 1 × 5 × 2 Monkhorst–Pack k-mesh was adopted for Brillouin zone integration.[23] DFT-D3 was used to account for the van der Waals interaction.[24] The reaction energy of lithiation-induced hydrogen evolution reaction (HER) was calculated as $E_{Li} = E(H_{2-x}Li_xTi_3O_7) + x·1/2\ E(H_2) - x·E(Li) - E(H_2Ti_3O_7)$, to evaluate the relative position of HER to Li^+/Li. The 1/2 H_2 reference is based on the computational hydrogen electrode approach,[25] while $E(Li)$ is the energy of the Li metal reference.

Differential Electrochemical Mass Spectrometry. Differential electrochemical mass spectrometry (DEMS) was performed on an $H_2Ti_3O_7$ electrode using the slurry preparation described above with a 3 mg mass loading on an Al coated fluorinated ethylene-propylene (FEP) membrane (50 μm thickness, Bohlender, Bola) as described previously.[26,27] In short, the active material covered membrane was cast on a perforated poly ether–ether–ketone (PEEK) plate, which was directly connected to the ultrahigh vacuum (UHV) chamber inlet of the mass spectrometer (Pfeiffer Vacuum QMA 410) for direct (without using a carrier gas) monitoring of the gas evolution rate upon cycling. The measurements were conducted in a half-cell configuration with Li metal strips as counter and reference electrodes, filled with 0.5 mL PC + 1.0 M $LiClO_4$ electrolyte ($LiClO_4$ anhydrous 99%; propylene carbonate, 99.5%, anhydrous, both from Thermo Scientific Chemicals). Prior to the measurements, the cell was allowed to rest for at least 6 h to achieve stable background signals of the selected ion currents and a stable open circuit potential. The electrochemical measurements were performed using a Princeton Research Instruments (PAR) 263 A potentiostat at a potential scan rate of 0.2 mV s^{-1}, or 0.03 mA galvanostatic discharging/charging in the potential range 1.0–3.0 V vs Li/Li^+, simultaneously recording the MS ion currents. The DEMS cell was assembled and operated in an Ar filled glovebox (LabMaster Pro, MBraun, oxygen and water content <0.1 ppm). The CO_2 and H_2 mass spectrometric signals were calibrated in separate experiments using formic acid oxidation (for CO_2 evolution) and hydrogen evolution over a sputtered Pt film electrode onto the same type of membrane in an aqueous electrolyte, 0.5 M H_2SO_4.

RESULTS AND DISCUSSION

Structure of Hydrogen Titanates. The crystal structures of the HTOs ($H_2Ti_yO_{2y+1}$; y = 3, 4, and 5) have monoclinic, $C2/m$, space group symmetry comprised of units of edge-sharing TiO_6 octahedra connected to the next unit via corner-sharing octahedra, forming a step-like structure with protons bound to bridging and terminal oxygens within the interlayer. HTOs can be distinguished by the number of edge-sharing octahedra within the layer: $H_2Ti_3O_7$ represents the 3-step HTO (3s-HTO) with three edge-sharing TiO_6 octahedra per unit, $H_2Ti_4O_9·nH_2O$ is the 4-step HTO (4s-HTO) with four edge-sharing octahedra, and $H_2Ti_5O_{11}·nH_2O$ is the 5-step HTO (5s-HTO) with five edge-sharing octahedra. The degree of interlayer protonation decreases with the HTO step size. Therefore, the interlayer environment can be modified by synthesizing HTOs with different step sizes.

The morphology of the synthesized HTOs consists of micron-sized rod-like particles, comparable to the morphology of the precursor alkali titanate (Figure 1b,c,e,f,h,i). The 3s-HTO has the lowest BET surface area of 5 $m^2\ g^{-1}$, while the 4s-HTO has the highest surface area of 33 $m^2\ g^{-1}$. XRD of the alkali titanate precursors can be well fit to previously reported crystal structures (Figure S3). $Cs_2Ti_5O_{11}$ closely fits a hydrated structure, possibly due to the uptake of ambient moisture. The 3s-HTO has an interlayer spacing of ~7.9 Å calculated from the 200 peak at 11.2° 2θ (Figure 2a). XRD data of the 4s-HTO and 5s-HTO show larger interlayer spacings of ~8.72 and 10.45 Å, respectively, along with a significant loss of intensity for reflections at higher angles, suggesting significant preferred orientation along the h00 planes (Figure 2a). Pawley refinements of the 4s-HTO (Figure S4) match the structure reported for $H_2Ti_4O_9·1.9H_2O$, as well as a second, more hydrated phase (>1.9 H_2O). Similarly, the XRD pattern for the 5s-HTO could be fit with two different hydrated phases, $H_2Ti_5O_{11}·3H_2O$ and $H_2Ti_5O_{11}·H_2O$ (Figure S5). Raman spectroscopy for all three HTOs shows Ti–O stretching modes between 700 and 900 cm^{-1} (Figure 2b). The positions of these Ti–O modes vary with the nature of the interlayer species, i.e., whether protons or alkali cations reside in the interlayer.[9,28] Slight shifts and intensity changes in the Ti–O stretching modes are observed across the alkali and protonated titanate counterparts (Figure S6a–c). We hypothesize that this is due to the change in bonding from ionic to covalent as the alkali cations are replaced with protons. The 3s-HTO displays two Ti–O stretching modes at 786 and 863 cm^{-1}, suggesting two bonding environments related to terminal and bridging oxygens, respectively. On the other hand, 4s- and 5s-HTO exhibit only one mode near 872 cm^{-1}; the absence of a

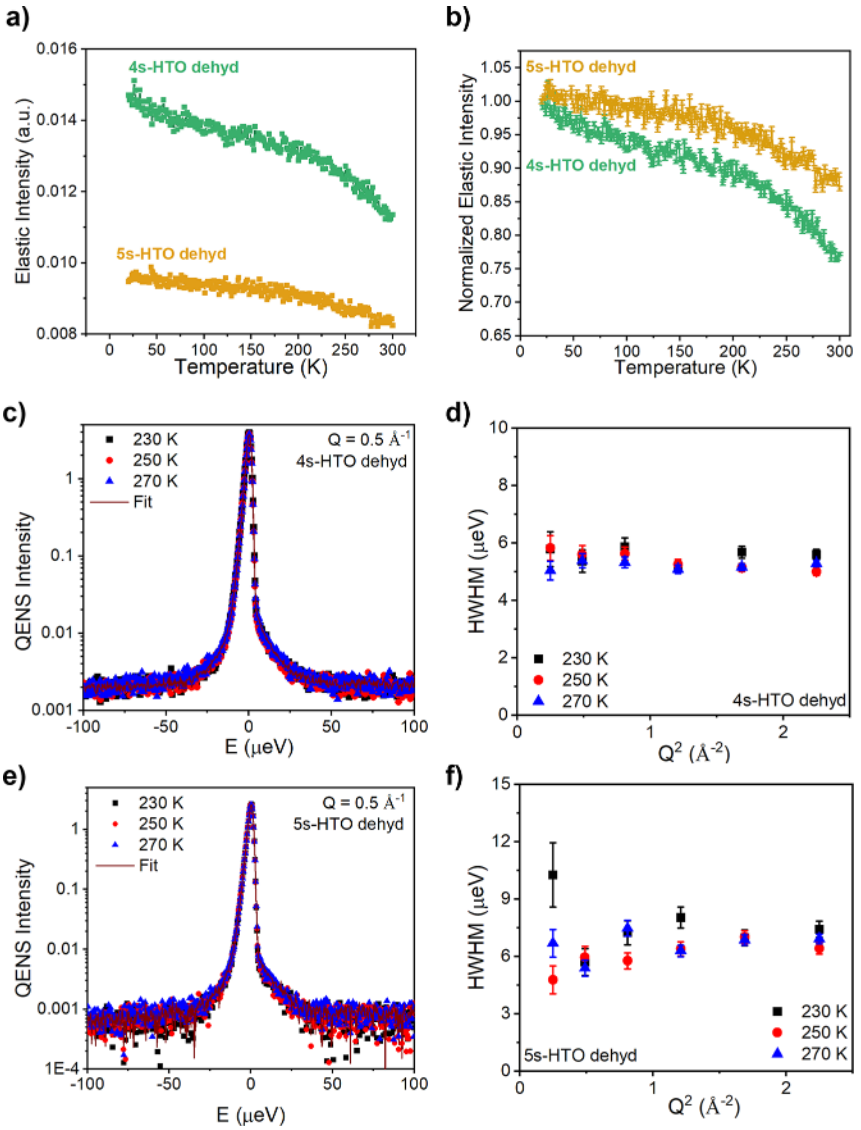

Figure 3. Q-averaged (integrated over the Q range of 0.2−2 $Å^{-1}$) elastic neutron scattering intensity as a function of temperature for dehydrated 4s-HTO and 5s-HTO (a) raw and (b) intensity normalized to the baseline temperature (T = 20 K). QENS spectra collected at 230, 250 and 270 K together with the model fit of dehydrated 4s-HTO (c) and dehydrated 5s-HTO (e). HWHM extracted from a single Lorentzian fit of the quasi-elastic signal of the dehydrated 4s-HTO (d) and dehydrated 5s-HTO (f). To compare the dynamics of the structural protons without contributions from the interlayer water, QENS data of the dehydrated 4s- and 5s-HTO are shown here. Additional data for the hydrated samples are shown in Figures S8−S10.

noticeable Ti−O stretch near 780 cm^{-1} in the larger step sizes may be related to the distribution of terminal and bridging oxygen environments, with there being fewer terminal sites in the 4s- and 5s-HTO as compared to 3s-HTO.

We performed thermogravimetric analysis (TGA) to determine the proton and water content of the HTOs (Figure 2c). The 3s-HTO shows initial dehydration beginning at 200 °C, with a 3.1 wt % mass loss up to 300 °C. This is near the theoretical removal of 0.5 H_2O to form $H_2Ti_6O_{12}$.[7,9,22] By 500 °C, the 3s-HTO shows a 5.4 wt % mass loss associated with roughly 0.78 H_2O. Prior work shows that annealing at high temperatures for longer times results in the complete removal of 1 H_2O from the 3s-HTO, forming $3TiO_2$(B).[7,9] The 4s-HTO and 5s-HTO show an initial 6% decrease in mass at low temperatures (<74 °C), followed by a more gradual mass loss until 500 °C. Both regions are attributed to the removal of interlayer water. The TGA results indicate the presence of 2 H_2O molecules within the interlayer of 4s-HTO and 2.42 H_2O molecules within the 5s-HTO. In situ heating XRD (Figure S7) also shows the dehydration of 4s- and 5s-HTO at temperatures <100 °C with a structural change of the 4s-HTO at 40 °C and the 5s-HTO at 65 °C. In situ XRD suggests that upon dehydration at 40 °C, 4s-HTO exhibits a contraction of the (200) interplanar distance. Prior studies report that heating to higher temperatures results in structural dehydration of the 4s-HTO to $H_2Ti_8O_{17}$, shown in Figure S7a at 80 °C.[6] Similarly, we hypothesize that the 5s-HTO (Figure S7b) begins to undergo dehydration at 65 °C, however we were not able to obtain high quality refinements of these structures. Pawley refinements performed on the pristine materials suggest the presence of $1.9 < n < 2.1$ interlayer waters for 4s-HTO and $1 < n < 3$ interlayer waters for the 5s-HTO (Figures S4 and S5). Upon preparing electrodes, the amount of interlayer water decreases (Figure S7c). We expect that the interlayer water in

the 4s-HTO and 5s-HTO is partially removed in the nonaqueous electrolyte during electrochemical cycling. The thermal and chemical dehydration steps for all three materials are shown in Figure S7c.

We utilized QENS to probe the dynamics of interlayer protons in 4s- and 5s-HTO. Our prior QENS studies on 3s-HTO revealed very weak temperature and Q-dependence of the width of QENS signals, indicating no translational motion of the protons on the time scale probed by QENS (0.006−0.4 ns).[9] In the current study, QENS of the dehydrated 4s- and 5s-HTO also reveal similar temperature and Q-dependence (see SI for QENS data analysis details) trends of half width at half-maximum (hwhm) of the QENS spectra (Figure 3c,e) as in the previously measured 3s-HTO. Dehydrated 4s-HTO has similar proton mobility (Figure 3d,f) but a higher fraction of mobile protons (Figure S8) than dehydrated 5s-HTO. The higher fraction of mobile protons in the 4s-HTO sample is also evident from the elastic neutron scattering intensity presented in Figure 3b. This indicates that 4s-HTO has a higher Brønsted acidity (lower pK_a) than the dehydrated 5s-HTO. However, the hydrated HTOs show an opposite trend compared to their dehydrated counterparts, exhibiting a higher fraction of mobile protons in 5s-HTO (Figures S8c and S10) than in 4s-HTO, while 4s-HTO exhibits the highest elastic intensity at a baseline temperature (Figure S8a). The complexity of the interlayer of these materials makes it challenging to deconvolute the contributions to the elastic neutron scattering intensity. Still, these differences may be due to the presence of higher amounts of surface water on the 4s-HTO because of its high surface area (Table 1), thus leading to a higher elastic intensity. Additionally, the higher degree of interlayer water within the 5s-HTO may contribute to its higher fraction of mobile protons (Figures S8c and S10). The presence of the surface (captured by a narrow component and suggesting a long-range mobility) and interlayer water (represented by a broader component indicating a localized mobility) necessitates the use of a sum of two Lorentzian functions (see SI for details) to analyze the hydrated HTOs (Figure S9).

Table 1. Etched Alkali Cation, Edge-sharing Octahedra Step Size, and BET Surface Area Measurements of the Hydrogen Titanate Powders

alkali precursor cation, A^+	step size	material	HTO BET Surface area ($m^2\ g^{-1}$)
Na	3	$H_2Ti_3O_7$ (3s-HTO)	5
K	4	$H_2Ti_4O_9{\cdot}1.9H_2O$ (4s-HTO)	33
Cs	5	$H_2Ti_5O_{11}{\cdot}3H_2O$ (5s-HTO)	14

Electrochemical and Structural Characterization. Having established the structure and proton dynamics of the pristine HTOs, we performed cyclic voltammetry in 1.0 M $LiClO_4$ at 0.2 mV s^{-1} to study electrochemical Li^+ insertion as a function of the degree of interlayer protonation and water. Low temperatures were used during electrode processing to preserve as much as possible the volatile interlayer water. The alkali titanate precursors show a low current response and specific capacities ≤10 mAh g^{-1} (Figure 4a), while the HTOs demonstrate higher electrochemical activity (by approximately a factor of 10), with multiple peaks in the probed potential range and higher specific capacities. At 0.2 mV s^{-1}, 3s-HTO has an anodic capacity of 118 mAh g^{-1} (~1.1 e^- per 3s-HTO), 4s-HTO of 142 mAh g^{-1} (~1.8 e^- per 4s-HTO), and 5s-HTO of 105 mAh g^{-1} (~1.6 e^- per 5s-HTO). The number of

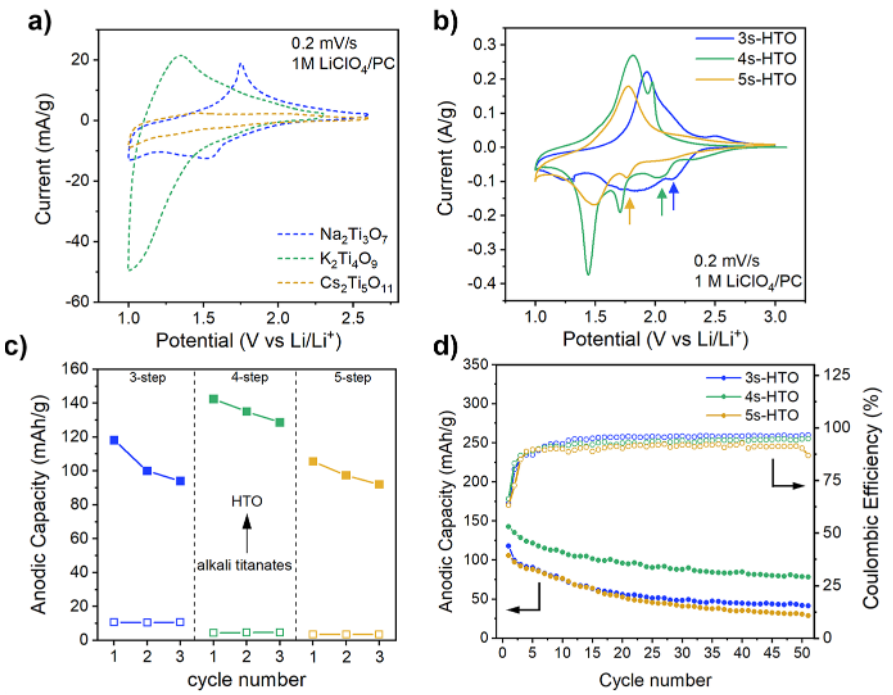

Figure 4. Electrochemical cycling of titanates in 1.0 M $LiClO_4$/PC at 0.2 mV s^{-1}. (a) CVs of the first cycle of alkali titanates at 0.2 mV s^{-1}. (b) CVs of the first cycle of 3s-HTO (blue), 4s-HTO (green), and 5s-HTO (yellow); arrows indicate irreversible cathodic peaks in the HTOs. (c) Comparison of the specific cathodic capacity (mAh g^{-1}) for alkali titanates and HTOs for the first three cycles. (d) Anodic capacity and Coulombic efficiency (%) as a function of cycle number for the HTOs.

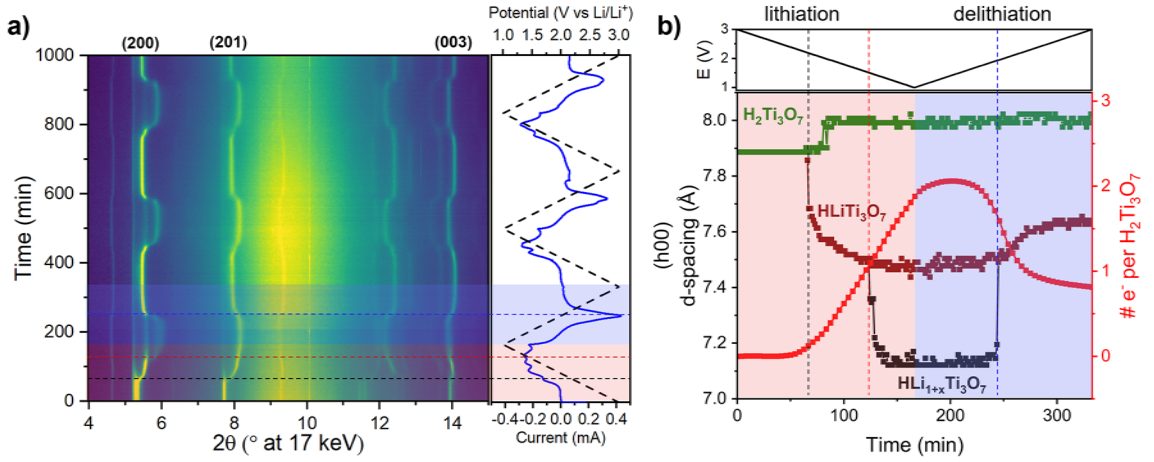

Figure 5. Operando electrochemical XRD of $H_2Ti_3O_7$. (a) Synchrotron XRD contour plot of $H_2Ti_3O_7$ in 1.0 M $LiClO_4$ in PC at 0.2 mV s^{-1} for three cycles. Dashed line at time ~75 min represents the irreversible phase transformation during Li^+ insertion at 2.25 V vs Li/Li^+ during the first cycle. Applied potential as a function of time is depicted by the black dashed line and the solid blue line shows the resulting current. (b) (h00) d-spacing of $H_2Ti_3O_7$ (green), $HLiTi_3O_7$ (maroon), and $HLi_{1+x}Ti_3O_7$ (black), and # of electrons per formula unit (red) as a function of time for the first cycle. Shaded red regions are the responses during Li^+ insertion (cathodic sweep), while the shaded blue areas show the response during Li^+ deinsertion (anodic sweep).

electrons were calculated per formula unit of HTO; for hydrated structures (4s- and 5s-HTO), we used the composition after electrode processing. The formula units were $H_2Ti_3O_7$ (3s-HTO), $H_2Ti_4O_9$ (4s-HTO), and $H_2Ti_5O_{11}\cdot H_2O$ (5s-HTO). This indicates that structural protons are necessary for high Li^+ insertion capacity (Figure 4b,c). The first cycle of the HTOs shows multiple peaks (Figure 4b). To assess the stability of the HTOs, we performed cyclic voltammetry for 50 cycles (Figure S11) Progressive cycling of the 3s-HTO reveals the decline and disappearance of some cathodic peaks and the retention of a cathodic peak near 1.5 V (Figure S11a), with similar changes observed in the 4s- and 5s-HTOs. For many titanate oxide materials, $Ti^{4+/3+}$ redox should occur between 1.5 and 1.75 V vs Li/Li^+ during Li^+ insertion.[22] While this is observed in our HTOs (Figure S11), the presence of additional irreversible peaks during reduction leads us to suspect the redox of other species, such as the structural protons or interlayer water. We tracked changes in anodic capacity and Coulombic efficiency (CE)—with CE calculated as the ratio of the anodic capacity to the cathodic capacity—during extended cycling (Figure 4d). The low CE during the initial cycles across all three materials is attributed to the contribution of reduction events that are present only in the initial cycles. Subsequent cycling leads to a plateau of the CEs near 100%. Similarly, the anodic capacity shows increased values during initial cycling, followed by a gradual capacity decay across the remaining cycles. These results indicate irreversible structural changes of the titanates during electrochemical cycling in a Li^+ electrolyte, which we probed further with operando XRD.

To unravel the structural transformations of the HTOs induced by Li^+ insertion, we performed operando synchrotron XRD during cyclic voltammetry at 0.2 mV s^{-1}. Figure 5a shows the XRD contour plots of the 3s-HTO as a function of time and potential (see Figure S13 for data across the entire 2θ range). During the first cathodic cycle, changes in the (200) and (201) reflections at ~2.25 V suggest an irreversible phase transition (black dotted line). We hypothesize that this irreversible change is due to the formation of a metastable $HLiTi_3O_7$ phase. At lower potentials (1 V vs Li/Li^+), we observe the formation of new peaks at higher degrees 2θ which we attribute to a more lithiated $HLi_{1+x}Ti_3O_7$ phase (red dotted line). Detailed changes in the (h00) d-spacing as a function of time and the number of electrons transferred to the electrode can be seen in Figure 5b. Subsequent cycles show relatively reversible structural changes, with the major phase having a (200) d-spacing of 7.6 Å. Peak shifts are also observed for the in-plane (003) reflection, suggesting a reorganization of the titanate layers during Li^+ insertion.

Based on cyclic voltammetry and operando XRD, we propose the following dominant mechanism for the initial reduction of 3s-HTO in a nonaqueous Li^+ electrolyte in the first cycle:

$$H_2Ti_3O_{7(s)} + Li^+_{(l)} + e^- \rightarrow \frac{1}{2}H_{2(g)} + HLiTi_3O_{7(s)}$$
$$E_{red} = 2.2 - 1.8 \text{ V vs } Li/Li^+ \quad (1)$$

$$HLiTi_3O_{7(s)} + Li^+_{(l)} + e^- \rightarrow HLi_{1+x}Ti_3O_{7(s)}$$
$$E_{red} < 1.8 \text{ V vs } Li/Li^+ \quad (2)$$

We hypothesize that the cathodic peaks at 2.2 and 1.8 V are due to the reduction of structural protons in 3s-HTO to H_2 gas, with cycling below 1.8 V leading to the formation of a more lithiated phase (eqs 1 and 2). Long-term cycling leads to continuous hydrogen evolution of the remaining protons and the formation of a metastable $HLiTi_3O_7$ phase, which is electrochemically active for reversible Li^+-insertion on subsequent cycles with redox involving $Ti^{4+/3+}$. Table S2 shows the cumulative irreversible capacity after the first and 50th cycle for each of the HTOs. The largest irreversible capacity is after the first cycle, corresponding to 0.64, 0.92, and 0.99 e^- per HTO formula unit. After 50 cycles, the cumulative irreversible capacity reaches 2.6 (3s-HTO), 6.0 (4s-HTO), and 5.9 (5s-HTO) e^- per formula unit. After one cycle, the 3s-HTO was <2 e^-/H^+ per formula unit due to residual H remaining within the interlayer, resulting in a final $HLiTi_3O_7$

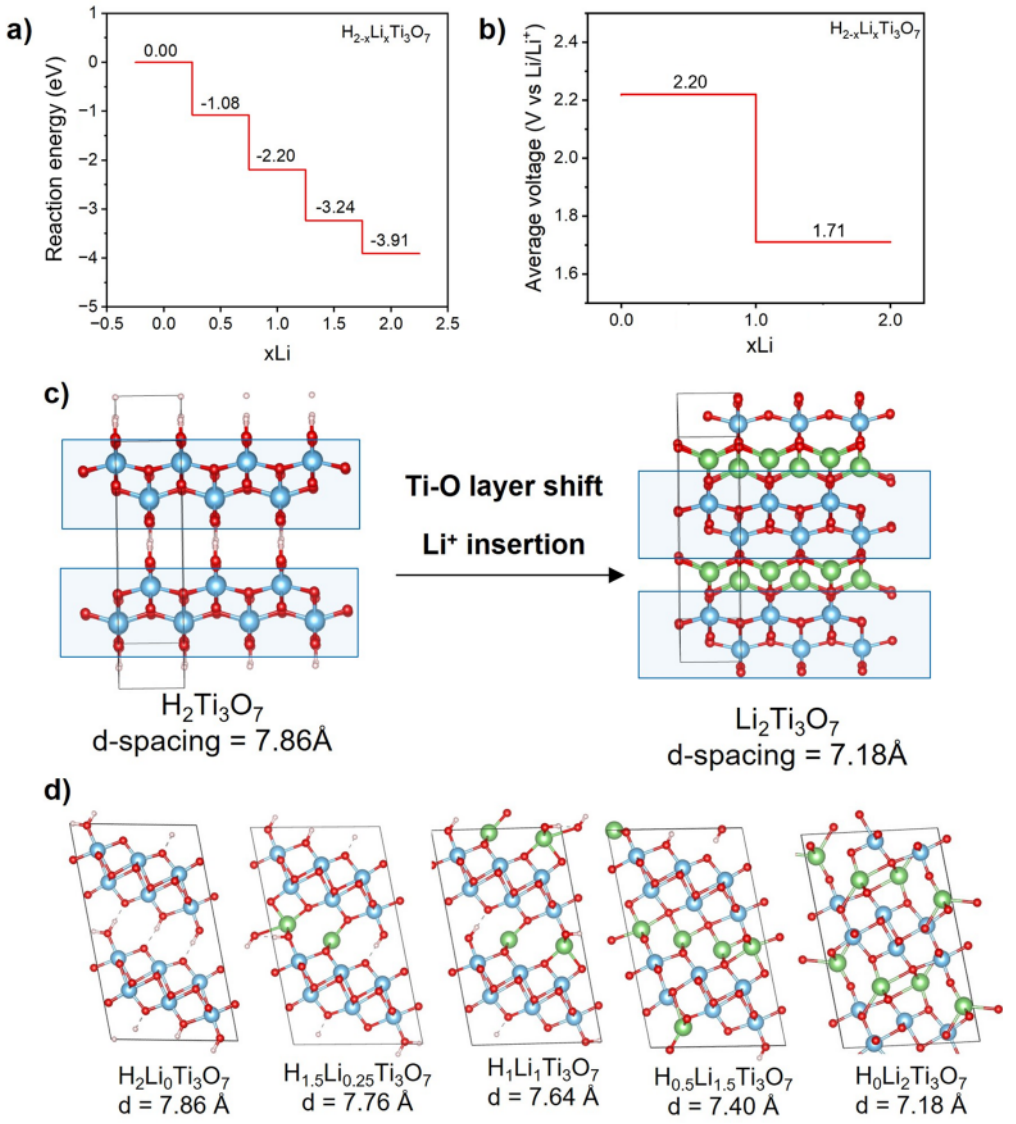

Figure 6. (a) DFT-computed reaction energy of $H_2Ti_3O_7$ + xLi (s) → $H_{2-x}Li_xTi_3O_7$ + 1/2 $x$$H_2$ (g) for x from 0 to 2. (b) Voltage profile for first/second half lithiation step. (c) DFT-calculated structures of $H_2Ti_3O_7$ and $Li_2Ti_3O_7$ showing a shift in the Ti−O layer to accommodate full Li^+ insertion. (d) Models for partially lithiated titanate from $H_2Li_0Ti_3O_7$ to $H_0Li_2Ti_3O_7$ (Ti: blue; Li: green; H: white; O: red).

structure. Both the 4s-HTO and 5s-HTO had close to 1 e^-/H^+ per formula unit after one cycle. After 50 cycles, all three materials report irreversible capacities greater than the expected $2e^-$ for the complete reduction of all structural protons. In the case of 4s- and 5s-HTO, reduction of interlayer water could result in these higher values.

We hypothesize that both processes, irreversible reduction of structural protons and reversible lithiation, overlap to some extent. This is based on the observed anodic capacity in the first cycle, which likely originates from (reversible) delithiation. However, the irreversible part of the cathodic capacity indicated by low Coulombic efficiencies (ca. 65% for first cycle) is assigned to the dominant solid-state proton reduction mechanism particularly during the first cycles. Similar irreversible structural changes were observed during Na^+ insertion in $H_2Ti_3O_7$, and Li^+ insertion into other protonated metal oxides.[4,29] Pérez-Flores et al. reported irreversible Li^+ insertion capacity after the first discharge cycle of an $H_2Ti_6O_{13}$ electrode, hypothesizing the formation of $Li_2Ti_6O_{13}$ through the reduction of protons to form H_2.[5] Although, to the best of our knowledge, there have been no reports monitoring the real-time irreversible structural changes and the formation of H_2 during Li^+ (de)insertion. To determine whether Li^+ insertion is necessary to promote bulk H_2 formation, we cycled 3s-HTO in a nonaqueous electrolyte containing a bulky cation (tetrabutylammonium). The CV shows no irreversible cathodic peak at high potentials (Figure S12), suggesting the importance of the charge-compensating ion for this structural transformation.

We also performed operando XRD for 4s-HTO and 5s-HTO (Figures S14 and S15). The 4s-HTO data revealed a different structure than $H_2Ti_4O_9{\cdot}1.9H_2O$, which was used to prepare the slurry electrode. Structural analysis showed better peak fitting with $H_2Ti_8O_{17}$—a titanate structure with more interconnected layers—which was likely formed upon dehydration of $H_2Ti_4O_9$ during electrode processing.[14] Due to the increased interconnections between layers, the 4s-HTO exhibits more minor—yet noticeable—interlayer contraction and expansion during respective Li^+ insertion and deinsertion (Figure S14). Interestingly, the 4s-HTO still experiences in-

plane shifts as indicated by the change in the (003) peak during ion insertion, suggesting a reorganization of the titanate layers similar to the 3s-HTO. The 5s-HTO shows shifts in the (200) peak, corresponding to the contraction of the interlayer upon insertion (Figure S15)—continued cycling results in decreased crystallinity and decreased peak intensity, especially for higher angle peaks. Plots of interlayer spacing and number of electrons as a function of time for all cycles are shown in Figure S16.

DFT calculations support the hypothesis that structural protons are reduced, and titanate layers undergo distortions during electrochemical cycling of 3s-HTO. The relative energy of $H_{2-x}Li_xTi_3O_7$ (where x = 0, 0.5, 1, 1.5, or 2) decreases with higher Li^+ content and less structural protons. Upon full lithiation to $Li_2Ti_3O_7$, the energy of the structure decreases to −3.91 eV relative to $H_2Ti_3O_7$ (Figure 6a). We further obtained the voltage profile required for full lithiation of HTO from the DFT energetics and found that the first and second lithiations have average voltages of 2.20 and 1.72 V, respectively (Figure 6b), which agrees with our estimates (eqs 1 and 2). The DFT results reveal that different energies are needed to reduce structural protons, which is in-line with the different potentials of the irreversible cathodic peaks during the first cycle of 3s-HTO. XRD patterns of the pristine 3s-HTO powder and electrode show small $Na_4Ti_5O_{12}$ impurities present from the unreacted precursor, although the major phase is still $H_2Ti_3O_7$ (Figure S17a,b). Upon oxidation to 3.0 V after the first, second, and third cycles, we observe the reversible formation of a new phase, with small amounts of $H_2Ti_3O_7$ still present (Figure S17c). Simulated XRD patterns for $HLiTi_3O_7$ match well with the observed patterns (Figure S17c, Table S3) suggesting partial reduction of the structural protons in 3s-HTO upon reduction. Comparisons of the XRD patterns at 1.0 and 3.0 V after the third cycle are shown in Figure S17d. At 1 V, $H_2Ti_3O_7$ and $HLiTi_3O_7$ are present, however, there is also a third, new phase, as evidenced by the new peak at 12.46° 2θ. This phase is formed reversibly upon reduction and indicates that electrochemical reduction of the partially lithiated $HLiTi_3O_7$ material is a two-phase (vs solid solution) process. We hypothesize that the new phase at 1.0 V has composition $HLi_{1+x}Ti_3O_7$, although we could not perform a refinement of the pattern at this stage. The new phase has a similar d-spacing to $Li_2Ti_3O_7$. DFT simulations show that a contraction of the interlayer spacing of 3s-HTO is expected upon lithiation. The source of this contraction is hypothesized to be from electrostatic attractive interactions between the Li^+ and the $[Ti_3O_7]^-$ layers and in-plane shifting of the titanate layers. DFT calculations show that a translational shift in the $[Ti_3O_7]^-$ layers is energetically favorable and leads to a decrease in the calculated interlayer spacing of ∼7.9 Å ($H_2Ti_3O_7$) to ∼7.1 Å ($Li_2Ti_3O_7$), with partial lithiation resulting in an interlayer spacing of ∼7.6 Å (Figure 6c,d). DFT calculations show that complete reduction of all structural protons is thermodynamically favored.

Differential Electrochemical Mass Spectrometry. We used differential electrochemical mass spectrometry (DEMS) to test our hypothesis of hydrogen evolution from bulk structural protons in the 3s-HTO by measuring the ion current for different gaseous species evolved during cyclic voltammetry. This technique was utilized for investigating volatile products at the electrode/electrolyte interface as a result of electrolyte degradation.[26] We find that 3s-HTO has evolution of both CO_2 and H_2 gas over three cycles, with each cycle evolving less H_2, especially upon sweeping to oxidizing potentials (Figures 7 and S19). The H_2 release could come

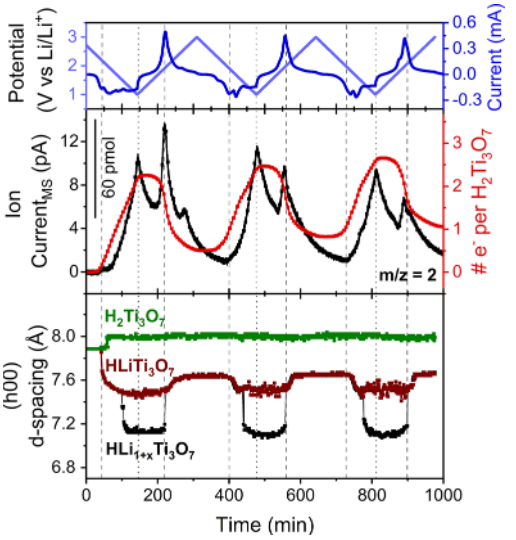

Figure 7. Differential electrochemical mass spectrometry (DEMS) of 3s-HTO cycled in 1.0 M $LiClO_4$ at 0.2 mV s^{-1}. Time-dependent plots of potential and electrochemical current (top plot), ion current for H_2 evolution and electron content per formula unit of $H_2Ti_3O_7$ (middle plot), and (h00) d-spacing obtained from operando XRD and electron content (bottom plot). d-spacing plot shows the potential dependence of the interlayer dynamics of $H_2Ti_3O_7$ (green), $HLiTi_3O_7$ (maroon), and $HLi_{1+x}Ti_3O_7$ (black). Gray dashed and dotted lines indicate d-spacing changes correlated with growth of H_2 ion current.

from different sources and here we identify two possibilities: the reduction of trace water from the electrolyte and the reduction of structural protons in 3s-HTO. Hydrogen formation at the lower potential limit during cathodic cycling does not decrease significantly with cycling and could indicate hydrogen formation from the reduction of trace water in the electrolyte. On the other hand, the peak-shaped hydrogen formation in the anodic scan, which fits the reoxidation peak in the 3s-HTO CV (Figure 7), and exhibits a gradual decay with cycling, strongly suggests hydrogen formation from the 3s-HTO, rather than from the electrolyte. We note that hydrogen formation can also appear at the Li counter electrode, as found from carrier gas driven online mass spectrometry measurements.[27,30,31] This can be neglected in the present membrane inlet DEMS setup. The CO_2 formation begins positive of ca. 1.5 V in the anodic scan, has an ill-resolved shoulder at ca. 1.9 V, and further increases to reach a peak at ca. 2.3 V, followed by a nearly constant CO_2 evolution rate in the following cathodic scan to 1.5 V, to decrease to the background level at lower potentials (Figure S19). The maximum CO_2 formation appears when the anodic current is only from the double layer current, which should not be the case with electrochemical oxidation of PC. This indicates a nonelectrochemical process for CO_2 formation. A gradual decrease of the CO_2 formation with cycling strongly suggests it originates from the electrode, rather than the electrolyte. We suspect the CO_2 evolution may be due to carbonate impurities on the surface or carbonate residues in the structure of the electrode. The latter is possible considering that Na_2CO_3 was used as a precursor in the 3s-HTO synthesis.

To gain further insights on the gas evolution and structural changes upon potential cycling of 3s-HTO, we overlaid the

DEMS and operando XRD data (Figure 7). We observe the onset of H_2 ion current after the *d*-spacing contraction near 2.2 V, followed by a continuous increase at potentials lower than 1.8 V. The initial decrease in H_2 ion current upon sweeping to higher potentials, followed by a sharp spike in H_2 at the moment of *d*-spacing re-expansion (1.9 V), is in agreement with the postulated formation of $HLi_{1+x}Ti_3O_7$. The behavior can be explained by H_2 evolution during the electrochemical reduction step with simultaneous H_2 confinement/storage in the contracted interlayer space. Upon the electrochemical oxidation step, the H_2 can be released along with deinsertion of the Li^+ ions. The CO_2 evolution occurs when there is a plateau in the interlayer spacing upon expansion back to 7.6 Å. This supports the above suggestion that CO_2 is released due to the structural transformation at potentials higher than ca. 2.2 V, rather than as an electrochemical reaction. The agreement of the electrochemical current with the ion currents plotted as a function of potential upon cycling can be more clearly seen in Figure S19. Follow-up DEMS experiments using galvanostatic cycling (Figure S20) showed more complex potential-dependent H_2 evolution events, possibly corresponding to structural transformations.

To verify that the changes observed from operando electrochemical XRD and DEMS measurements were indeed due to the removal of structural protons, ex situ ^1H and ^7Li SSNMR spectroscopy were performed on a fully lithiated slurry powder (Figure 8a,b). The 3s-HTO and the 3s-HTO

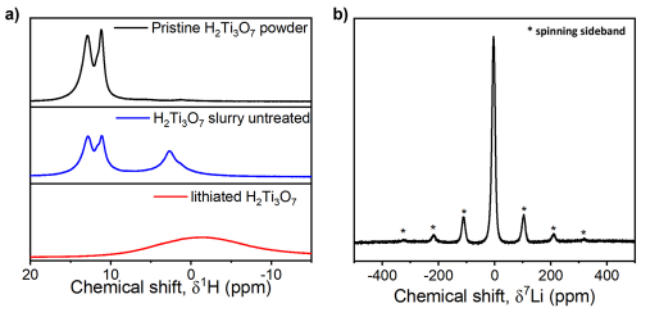

Figure 8. Ex situ solid-state NMR of $H_2Ti_3O_7$ before and after Li^+ insertion. (a) Solid-state ^1H NMR of pristine $H_2Ti_3O_7$ powder (black), $H_2Ti_3O_7$ dried slurry (blue), and $H_2Ti_3O_7$ after 10 cycles and holding at 1 V vs Li/Li^+ for 24 h in 1 M $LiClO_4$ in PC. (b) Solid-state ^7Li NMR of $H_2Ti_3O_7$ after 10 cycles and holding at 1 V vs Li/Li^+ for 24 h in 1 M $LiClO_4$ in PC.

slurry exhibits signals at 11.0 and 13.0 ppm, assigned structural protons.[4] The signal at 2.7 ppm observed in the slurry is attributed to residual NMP. After cycling to low potentials, ^1H NMR shows the complete disappearance of the structural proton peaks, while ^7Li NMR shows a high intensity Li peak. This high intensity peak is observed in lithiated titanate structures, such as $Li_4Ti_5O_{12}$ and $Li_2Ti_3O_7$, suggesting the formation of a lithium-rich titanate phase with lithium in the interlayer.[32,33] The broad signal observed in the lithiated slurry, which is centered at −1 ppm, is attributed to residual electrolyte solvent in the pores of carbon black. The observed signal shift and broadening is caused by the nuclear-independent chemical shift (NICS).[34,35] From this, we can conclude that the electrochemical reaction in a Li^+-non aqueous electrolyte led to the reduction and removal of interlayer protons. Ex situ XRD and Raman of 3s-HTO that was chemically lithiated and deprotonated in LiOH shows comparable changes in structure and bonding sites, with new reflections near the (200) and (201) peaks (Figure S21a,b).

Variations in HTO Proton Acidity. Finally, we consider how the chemical environment of the interlayer dictates the reduction potential for hydrogen formation from HTO. The decrease in the proton reduction potential with increasing step size (Figure 4b) suggests that the HTOs display higher proton bonding strengths with increasing step sizes and as a result, lower acidities: 3s-HTO would be the most acidic and 5s-HTO would be the least acidic. FTIR and ^1H NMR spectroscopy allow us to distinguish, respectively, changes in O···H bond lengths and acidities of structural protons. We observed broad O−H stretching vibrations between 2700−3500 cm^{-1} in the FTIR spectra (Figure S22a) for all the HTOs, with noticeable shifts of the O−H stretch to higher wavenumbers with increasing step sizes. Other minerals containing O−H···O bonds exhibit higher O−H stretching frequencies with increasing d(O···H) bond length.[36] These bond lengths have been proposed as key descriptors for proton transfer in solid acids.[37] It is important to note that the HTOs contain both covalent O−H bonds and H···O hydrogen bonds that bridge the titanate layers. This is represented in the DFT-calculated structure in Figure 9b. We propose that the protons in the 3s-

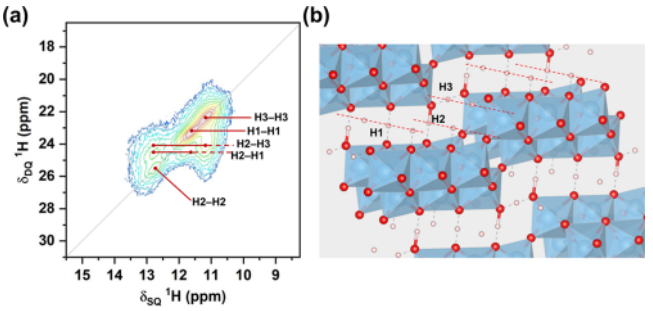

Figure 9. (a) T^1H-^1H DQ/SQ correlation NMR spectroscopy for pristine 3s-HTO powder. (b) DFT calculated structure of 3s-HTO. Red dashed line represents the *b*-axis alignment of hydrogen atoms.

HTO reside closer to the center of the interlayer with less bias toward a particular oxygen site. However, with increased *d*-spacing and the presence of interlayer water species, the structural protons in the 4s- and 5s-HTOs are hypothesized to experience a bias toward one oxygen site, with little-to-no bridging to an opposing oxygen. This is illustrated in Figure S23, showing the increase in O···H bond distances (gray dashed lines) with increasing interplanar distance. This is corroborated by the SS ^1H NMR of the HTO powders (Figure S19b) which shows lower ^1H chemical shifts for the 4s- and 5s-HTOs, suggesting their protons are more strongly associated toward a particular oxygen, and therefore less acidic. The signals from the ^1H NMR of 3s-HTO at 11.0 and 12.8 ppm can be respectively correlated to the 2775 and 3151 cm^{-1} O−H stretching frequencies in the FTIR, with the higher frequency corresponding to shorter O−H bonds and longer O···H bonds. Proton chemical shifts and FTIR O−H stretching modes for the HTOs are listed in Table S4. Signals from more acidic protons typically appear on the more deshielded side (exhibiting a more positive chemical shift), enabling comparison of the relative acidity of the different HTOs.[38] Figure 9a,b show the two-dimensional $^1H-^1H$ homonuclear double-quantum (DQ)/single-quantum (SQ) correlation spectrum and the crystal structure of $H_2Ti_3O_7$,

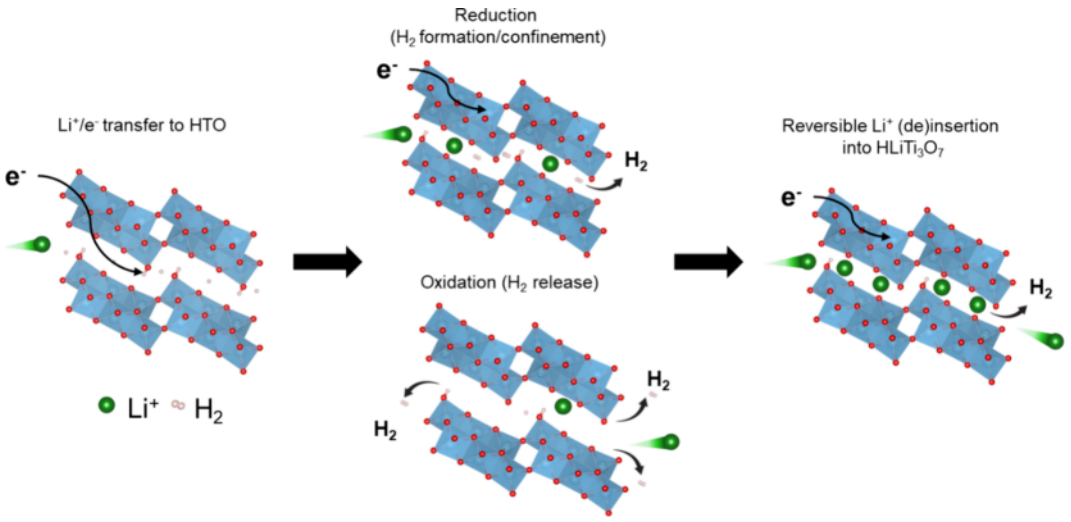

Figure 10. Proposed mechanism of hydrogen evolution from structural protons and electrochemical conversion of the 3s-HTO to $HLiTi_3O_7$.

respectively. The DQ/SQ spectrum revealed three types of protons at 11.1, 11.6, and 12.8 ppm and their proximities between H1−H1, H2−H2, H3−H3, H1−H2, and H2−H3. The proximity observed between equivalent protons is due to their proximity along the *b*-axis (represented by red dashed lines). The chemical shifts predicted from the DFT NMR calculation and the observed $^1H-^1H$ proximity identified protons corresponding to the three signals as shown in Figure 9b. This agrees with DFT calculations from previous studies showing the formation of both hydroxyl and water groups.[9] In this structure, the most acidic protons are coordinated to terminal oxygens (H2 in Figure 9b). Previous reports of the 3s-HTO show higher chemical shifts when compared to other hydrogen titanates, such as the ramsdellite structure of $H_2Ti_3O_7$ and the $H_2Ti_6O_{12}$ tunnel structure.[4,32,33] This is indicative of the higher acidity of the 3s-HTO. Similarly, it shows higher proton chemical shifts when compared to the 4s-HTO and 5s-HTO, suggesting that the latter two are less acidic. Interfacial water was also observed in the ^1H NMR for the 4s-HTO. The 4s-HTO and 5s-HTO, respectively, show signals for structural protons at 9.0 and 8.0 ppm (Figure S22b), which is consistent with our hypothesis that HTO acidity decreases with increasing step size. Acid titrations of the alkali titanates further corroborated the differences in proton affinities across the HTOs (see SI for more details). While differences in electronic conductivity can also result in such trends, DRS measurements show similar band gaps near 3.42 eV for all three HTOs (Figure S24). Figure 10 illustrates the proposed stepwise mechanism for hydrogen formation and conversion of the HTO to $HLiTi_3O_7$.

In all, this study presents a comprehensive characterization of the solid-state electrochemistry of a series of metastable HTOs in a nonaqueous, Li^+ electrolyte, and proposes a mechanism involving the reduction of interlayer protons dictated by their acidity. The results have implications beyond metastable HTOs due to the diversity of novel materials containing water or structural protons proposed for electrochemical energy storage in nonaqueous electrolytes. These include other hydrous oxides, framework materials like Prussian blue analogs, as well as 2D materials like MXenes.[39,40] Whether the materials contain structural protons or water, as in the case of the HTOs, or other types of solvent molecules, gas evolution measurements such as DEMS will be critical to understand the underlying electrochemical mechanisms. We hypothesize that this behavior is unique to nonaqueous electrolytes where no electrolyte water or proton species can compensate for the solid-state electrochemical reduction reactions. For example, in the case of HTOs in aqueous electrolytes, the degradation mechanism involves Ti^{3+} dissolution and competitive H_2 generation with protons sourced from the electrolyte. In the case of HTOs in nonaqueous electrolytes studied here, the mechanism also involves H_2 evolution but with protons sourced from the titanate and there is no Ti^{3+} dissolution but rather the formation of a lithium titanate. Electrochemical ion insertion is a critical part of the mechanism since we observed no significant redox activity when the electrolyte contained a noninserting cation (tetrabutylammonium). Second, our study is related to, though distinct, from other solid-state electrochemical reactions that do not involve electron transfer to/from a transition metal cation. Perhaps most prominent among these is the mechanism of anion redox observed in some layered alkali metal oxides cycled to oxidizing potentials. A recent computation study proposed that the O_2 evolved due to electron transfer from the oxygen anions remains trapped in the oxide structure, and undergoes reversible redox, because the structure does not allow for the transport of the O_2 gas and it thus remains confined within the lattice.[41] In our work with HTOs, we find that the greatest rate of H_2 evolution occurs during the anodic scan coincident with an expansion of the interlayer. This suggests that H_2 is confined to the interlayer upon its initial formation during electrochemical reduction and is only released when the structure allows.

CONCLUSIONS

This study provides a comprehensive understanding of the solid-state electrochemistry of layered HTOs in a nonaqueous Li^+ electrolyte. We show that the electrochemical mechanism involves Li^+ insertion and generation of H_2, and that the oxide acidity dictates the first reduction potential. By combining spectroscopic, structural, and electrochemical techniques, we correlate the relative acid strengths of the structural protons to the degree of structural change during Li^+ insertion. We determined that structural protons are critical for enabling high Li^+ insertion capacity. QENS and solid-state ^1H NMR

spectroscopy support the titration results, showing that the degree of proton uptake, and consequently, proton removal, is dependent on the structure of the metal oxide. Operando synchrotron XRD revealed that HTOs with more acidic protons undergo rapid, irreversible structural changes due to hydrogen evolution of structural protons, with 3s-HTO displaying irreversible changes at the highest reduction potentials, followed by 4s-HTO and 5s-HTO. Ex situ ^{1}H NMR revealed a loss of structural protons in the 3s-HTO after extended electrochemical cycling, suggesting these structural changes are likely attributed to the reduction of bulk protons. Finally, DEMS results showed evidence of H_2 evolution during both reductive and oxidative potentials, suggesting initial confinement of the H_2 gas during reduction. These results emphasize the significance of interlayer structural protons for Li^+ insertion into HTOs, opening the way for studying materials design factors such as the acidity of protonated metal oxides for next-generation ion-insertion coupled electron transfer materials for energy storage and conversion. The generalization of this H_2 evolution mechanism can provide insights into the dynamic behavior of other hydrated insertion hosts, such as MXenes and Prussian blue analogs. It also provides an example of an electrochemical insertion reaction that involves electron transfer to nonmetal ions, in analogy to anion redox in some layered alkali transition metal oxides.

AUTHOR INFORMATION

Corresponding Author

Veronica Augustyn − *Department of Materials Science and Engineering, North Carolina State University, Raleigh, North Carolina 27606, United States;* orcid.org/0000-0001-9885-2882; Email: vaugust@ncsu.edu

Authors

Saeed Saeed − *Department of Materials Science and Engineering, North Carolina State University, Raleigh, North Carolina 27606, United States*

Simon Fleischmann − *Department of Materials Science and Engineering, North Carolina State University, Raleigh, North Carolina 27606, United States; Helmholtz Institute Ulm (HIU) for Electrochemical Energy Storage, 89081 Ulm, Germany; Karlsruhe Institute of Technology, 76021 Karlsruhe, Germany;* orcid.org/0000-0001-9475-3692

Takeshi Kobayashi − *U.S. DoE Ames National Laboratory, Iowa State University, Ames, Iowa 50011, United States;* orcid.org/0000-0002-6366-0925

Zenonas Jusys − *Helmholtz Institute Ulm (HIU) for Electrochemical Energy Storage, 89081 Ulm, Germany; Karlsruhe Institute of Technology, 76021 Karlsruhe, Germany;* orcid.org/0000-0003-3970-5799

Eugene Mamontov − *Neutron Scattering Division, Oak Ridge National Laboratory, Oak Ridge, Tennessee 37831, United States;* orcid.org/0000-0002-5684-2675

Naresh C. Osti − *Neutron Scattering Division, Oak Ridge National Laboratory, Oak Ridge, Tennessee 37831, United States;* orcid.org/0000-0002-0213-2299

Noah P. Holzapfel − *Department of Materials Science and Engineering, North Carolina State University, Raleigh, North Carolina 27606, United States;* orcid.org/0000-0002-4566-4033

Haohong Song − *Interdisciplinary Materials Science Program, Vanderbilt University, Nashville, Tennessee 37235, United States*

Tao Wang − *Chemical Sciences Division, Oak Ridge National Laboratory, Oak Ridge, Tennessee 37831, United States;* orcid.org/0000-0001-5004-160X

Sheng Dai − *Chemical Sciences Division, Oak Ridge National Laboratory, Oak Ridge, Tennessee 37831, United States;* orcid.org/0000-0002-8046-3931

De-en Jiang − *Interdisciplinary Materials Science Program and Department of Chemical and Biomolecular Engineering, Vanderbilt University, Nashville, Tennessee 37235, United States;* orcid.org/0000-0001-5167-0731

Notes

The authors declare no competing financial interest.

ACKNOWLEDGMENTS

We thank Dr. Michael A. Spencer for acquiring SEM images of the pristine materials in this study. We also thank Dr. Nicholas Strange, Dr. Johanna Weker, and Charles L. Troxel for their help with the operando XRD experiments at SSRL. This work was supported as part of the Fluid Interface Reactions, Structure and Transport (FIRST), an Energy Frontiers Research Center funded by the U.S. Department of Energy, Office of Science, Office of Basic Energy. Experiments at ORNL's Spallation Neutron Source was sponsored by the Scientific User Facilities Division, Office of Basic Energy Sciences, U.S. Department of Energy. Oak Ridge National Laboratory is managed by UT-Battelle, LLC, for U.S. DOE under Contract No. DEAC05-00OR22725. Use of the Stanford Synchrotron Radiation Lightsource, SLAC National Accelerator Laboratory, is supported by the U.S. Department of Energy, Office of Science, Office of Basic Energy Sciences under Contract No. DE-AC02-76SF00515. This work was performed in part at the Analytical Instrumentation Facility (AIF) at North Carolina State University, which is supported by the State of North Carolina and the National Science Foundation (award # ECCS-2025064). The AIF is a member of the North Carolina Research Triangle Nanotechnology Network (RTNN), a site in the National Nanotechnology Coordinated Infrastructure (NNCI). The solid-state NMR experiments were performed at the Ames National Laboratory, which is operated for the U.S. DOE by Iowa State University under contract # DE-AC02-07CH11358. S.F. acknowledges funding from the German Federal Ministry of Education and

Research (BMBF) in the NanoMatFutur program (grant No. 03XP0423). S.F. and Z.J. acknowledge basic funding from the Helmholtz Association.

REFERENCES

(1) Augustyn, V.; Gogotsi, Y. 2D Materials with Nanoconfined Fluids for Electrochemical Energy Storage. *Joule* **2017**, *1* (3), 443−452.

(2) Han, S. D.; Kim, S.; Li, D.; Petkov, V.; Yoo, H. D.; Phillips, P. J.; Wang, H.; Kim, J. J.; More, K. L.; Key, B.; Klie, R. F.; Cabana, J.; Stamenkovic, V. R.; Fister, T. T.; Markovic, N. M.; Burrell, A. K.; Tepavcevic, S.; Vaughey, J. T. Mechanism of Zn Insertion into Nanostructured δ-MnO_2: A Nonaqueous Rechargeable Zn Metal Battery. *Chem. Mater.* **2017**, *29* (11), 4874−4884.

(3) Tepavcevic, S.; Liu, Y.; Zhou, D.; Lai, B.; Maser, J.; Zuo, X.; Chan, H.; Král, P.; Johnson, C. S.; Stamenkovic, V.; Markovic, N. M.; Rajh, T. Nanostructured Layered Cathode for Rechargeable Mg-Ion Batteries. *ACS Nano* **2015**, *9* (8), 8194−8205.

(4) Eguía-Barrio, A.; Castillo-Martínez, E.; Zarrabeitia, M.; Muñoz-Márquez, M. A.; Casas-Cabanas, M.; Rojo, T. Structure of $H_2Ti_3O_7$ and Its Evolution during Sodium Insertion as Anode for Na Ion Batteries. *Phys. Chem. Chem. Phys.* **2015**, *17* (10), 6988−6994.

(5) Pérez-Flores, J. C.; Baehtz, C.; Hoelzel, M.; Kuhn, A.; García-Alvarado, F. $H_2Ti_6O_{13}$, a New Protonated Titanate Prepared by Li^+/H^+ Ion Exchange: Synthesis, Crystal Structure and Electrochemical Li Insertion Properties. *RSC Adv.* **2012**, *2* (8), 3530−3540.

(6) Suzuki, S.; Miyayama, M. Lithium Intercalation Properties of Tetratitanates and Octatitanates. *J. Ceram. Soc. Japan* **2010**, *118* (1384), 1154−1158.

(7) Zhu, G. N.; Wang, C. X.; Xia, Y. Y. Structural Transformation of Layered Hydrogen Trititanate ($H_2Ti_3O_7$) to TiO_2(B) and Its Electrochemical Profile for Lithium-Ion Intercalation. *J. Power Sources* **2011**, *196* (5), 2848−2853.

(8) Fleischmann, S.; Pfeifer, K.; Widmaier, M.; Shim, H.; Budak, Ö.; Presser, V. Understanding Interlayer Deprotonation of Hydrogen Titanium Oxide for High-Power Electrochemical Energy Storage. *ACS Appl. Energy Mater.* **2019**, *2* (5), 3633−3641.

(9) Fleischmann, S.; Sun, Y.; Osti, N. C.; Wang, R.; Mamontov, E.; Jiang, D. E.; Augustyn, V. Interlayer Separation in Hydrogen Titanates Enables Electrochemical Proton Intercalation. *J. Mater. Chem. A* **2020**, *8* (1), 412−421.

(10) Kang, S.; Singh, A.; Reeves, K. G.; Badot, J. C.; Durand-Vidal, S.; Legein, C.; Body, M.; Dubrunfaut, O.; Borkiewicz, O. J.; Tremblay, B.; Laberty-Robert, C.; Dambournet, D. Hydronium Ions Stabilized in a Titanate-Layered Structure with High Ionic Conductivity: Application to Aqueous Proton Batteries. *Chem. Mater.* **2020**, *32*, 9458.

(11) Fortunato, J.; Shin, Y. K.; Spencer, M. A.; van Duin, A. C. T.; Augustyn, V. Choice of Electrolyte Impacts the Selectivity of Proton-Coupled Electrochemical Reactions on Hydrogen Titanate. *J. Phys. Chem. C* **2023**, *127* (25), 11810−11821.

(12) Sasaki, T.; Watanabe, M.; Komatsu, Y.; Fujiki, Y. Layered Hydrous Titanium Dioxide: Potassium Ion Exchange and Structural Characterization. *Inorg. Chem.* **1985**, *24* (14), 2265−2271.

(13) Sasaki, T.; Komatsu, Y.; Fujiki, Y. Protonated Pentatitanate: Preparation, Characterizations, and Cation Intercalation. *Chem. Mater.* **1992**, *4* (4), 894−899.

(14) Izawa, H.; Kikkawa, S.; Koizumi, M. Ion Exchange and Dehydration of Layered Titanates, $Na_2Ti_3O_7$ and $K_2Ti_4O_9$. *J. Phys. Chem.* **1982**, *86* (25), 5023−5026.

(15) Mamontov, E.; Herwig, K. W. A Time-of-Flight Backscattering Spectrometer at the Spallation Neutron Source, BASIS. *Rev. Sci. Instrum.* **2011**, *82* (8), No. 085109.

(16) Arnold, O.; Bilheux, J. C.; Borreguero, J. M.; Buts, A.; Campbell, S. I.; Chapon, L.; Doucet, M.; Draper, N.; Ferraz Leal, R.; Gigg, M. A.; Lynch, V. E.; Markvardsen, A.; Mikkelson, D. J.; Mikkelson, R. L.; Miller, R.; Palmen, K.; Parker, P.; Passos, G.; Perring, T. G.; Peterson, P. F.; Ren, S.; Reuter, M. A.; Savici, A. T.; Taylor, J. W.; Taylor, R. J.; Tolchenov, R.; Zhou, W.; Zikovsky, J. Mantid - Data Analysis and Visualization Package for Neutron Scattering and μ SR Experiments. *Nucl. Instruments Methods Phys. Res. Sect. A Accel. Spectrometers, Detect. Assoc. Equip.* **2014**, *764*, 156−166.

(17) Ramirez-Cuesta, A.; Smith, R.; Mamontov, E.; Cheng, Y. ICE-MAN the Integrated Computational Environment for Modeling and Analysis for Neutrons at ORNL. *EPJ. Web Conf.* **2022**, *272*, No. 01013.

(18) Kresse, G.; Furthmüller, J. Efficiency of Ab-Initio Total Energy Calculations for Metals and Semiconductors Using a Plane-Wave Basis Set. *Comput. Mater. Sci.* **1996**, *6*, 15−50.

(19) Kresse, G.; Furthmüller, J. Efficient Iterative Schemes for Ab Initio Total-Energy Calculations Using a Plane-Wave Basis Set. *Phys. Rev. B* **1996**, *54*, 11169−11186.

(20) Perdew, J. P.; Burke, K.; Ernzerhof, M. Generalized Gradient Approximation Made Simple. *Phys. Rev. Lett.* **1996**, *77*, 3865−3868.

(21) Blöchl, P. E. Projector Augmented-Wave Method. *Phys. Rev. B* **1994**, *50*, 17953−17979.

(22) Rousse, G.; Arroyo-De Dompablo, M. E.; Senguttuvan, P.; Ponrouch, A.; Tarascon, J. M.; Palacín, M. R. Rationalization of Intercalation Potential and Redox Mechanism for $A_2Ti_3O_7$ (A = Li, Na). *Chem. Mater.* **2013**, *25* (24), 4946−4956.

(23) Monkhorst, H. J.; Pack, J. D. Special Points for Brillouin-Zone Integrations. *Phys. Rev. B* **1976**, *13*, 5188.

(24) Grimme, S.; Antony, J.; Ehrlich, S.; Krieg, H. A Consistent and Accurate Ab Initio Parametrization of Density Functional Dispersion Correction (DFT-D) for the 94 Elements H-Pu. *J. Chem. Phys.* **2010**, *132* (15), 154104.

(25) Nørskov, J. K.; Rossmeisl, J.; Logadottir, A.; Lindqvist, L.; Kitchin, J. R.; Bligaard, T.; Jónsson, H. Origin of the Overpotential for Oxygen Reduction at a Fuel-Cell Cathode. *J. Phys. Chem. B* **2004**, *108* (46), 17886−17892.

(26) Jusys, Z.; Binder, M.; Schnaidt, J.; Behm, R. J. A Novel DEMS Approach for Studying Gas Evolution at Battery-Type Electrode|electrolyte Interfaces: High-Voltage $LiNi_{0.5}Mn_{1.5}O_4$ Cathode in Ethylene and Dimethyl Carbonate Electrolytes. *Electrochim. Acta* **2019**, *314*, 188−201.

(27) Klein, F.; Bansmann, J.; Jusys, Z.; Pfeifer, C.; Scheitenberger, P.; Mundszinger, M.; Geiger, D.; Biskupek, J.; Kaiser, U.; Behm, R. J.; Lindén, M.; Wohlfahrt-Mehrens, M.; Axmann, P. Enhanced Electrochemical Capacity of Spherical Co-Free $Li_{1.2}Mn_{0.6}Ni_{0.2}O_2$ Particles after a Water and Acid Treatment and Its Influence on the Initial Gas Evolution Behavior. *ChemSusChem* **2022**, *15*, No. e202201061.

(28) Byeon, S. H.; Lee, S. O.; Kim, H. Structure and Raman Spectra of Layered Titanium Oxides. *J. Solid State Chem.* **1997**, *130* (1), 110−116.

(29) Miranda, J.; Le Calvez, E.; Retoux, R.; Crosnier, O.; Brousse, T. Revisiting $Rb_2TiNb_6O_{18}$ as Electrode Materials for Energy Storage Devices. *Electrochem. Commun.* **2022**, *137*, No. 107249.

(30) Michalak, B.; Berkes, B. B.; Sommer, H.; Brezesinski, T.; Janek, J. Electrochemical Cross-Talk Leading to Gas Evolution and Capacity Fade in $LiNi_{0.5}Mn_{1.5}O_4$/Graphite Full-Cells. *J. Phys. Chem. C* **2017**, *121* (1), 211−216.

(31) Metzger, M.; Strehle, B.; Solchenbach, S.; Gasteiger, H. A. Origin of H_2 Evolution in LIBs: H_2O Reduction vs. Electrolyte Oxidation. *J. Electrochem. Soc.* **2016**, *163* (5), A798−A809.

(32) Odziomek, M.; Chaput, F.; Lerouge, F.; Rutkowska, A.; Świerczek, K.; Carlier, D.; Sitarz, M.; Parola, S. Impact of the Synthesis Parameters on the Microstructure of Nano-Structured LTO Prepared by Glycothermal Routes and ^{7}Li NMR Structural Investigations. *J. Sol-Gel Sci. Technol.* **2019**, *89* (1), 225−233.

(33) Orera, A.; Azcondo, M. T.; García-Alvarado, F.; Sanz, J.; Sobrados, I.; Rodríguez-Carvajal, J.; Amador, U. Insight into Ramsdellite $Li_2Ti_3O_7$ and Its Proton-Exchange Derivative. *Inorg. Chem.* **2009**, *48* (16), 7659−7666.

(34) Lazzeretti, P. Ring Currents. *Prog. Nucl. Magn. Reson. Spectrosc.* **2000**, *36* (1), 1−88.

(35) Cui, J.; Lin, X.; Zhao, W.; Cummings, P. T.; Pruski, M.; Kobayashi, T. NMR and Theoretical Study of In-Pore Diffusivity of

Ionic Liquid-Solvent Mixtures. *J. Phys. Chem. B* **2022**, *126* (26), 4889−4898.
(36) Libowitzky, E. Correlation of O-H Stretching Frequencies and O-H···O Hydrogen Bond Lengths in Minerals. *Monatshefte fur Chemie* **1999**, *130* (8), 1047−1059.
(37) Žguns, P.; Klyukin, K.; Wang, L. S.; Xiong, G.; Li, J.; Haile, S. M.; Yildiz, B. Uncovering Fast Solid-Acid Proton Conductors Based on Dynamics of Polyanion Groups and Proton Bonding Strength. *Energy Environ. Sci.* **2024**, *17*, 5730−5742.
(38) Zhu, L.; Gu, Q.; Sun, P.; Chen, W.; Wang, X.; Xue, G. Characterization of the Mobility and Reactivity of Water Molecules on TiO 2 Nanoparticles by ^{1}H Solid-State Nuclear Magnetic Resonance. *ACS Appl. Mater. Interfaces* **2013**, *5* (20), 10352−10356.
(39) Dreyer, S. L.; Maddar, F. M.; Kondrakov, A.; Janek, J.; Hasa, I.; Brezesinski, T. Elucidating Gas Evolution of Prussian White Cathodes for Sodium-Ion Battery Application: The Effect of Electrolyte and Moisture. *Batter. Supercaps* **2024**, *7* (4), No. e202300595.
(40) He, Y.; Dreyer, S. L.; Ting, Y.; Ma, Y.; Hu, Y.; Goonetilleke, D.; Tang, Y.; Diemant, T.; Zhou, B.; Kowalski, P. M.; Fichtner, M.; Hahn, H.; Aghassi-Hagmann, J.; Brezesinski, T.; Breitung, B.; Ma, Y. Entropy-Mediated Stable Structural Evolution of Prussian White Cathodes for Long-Life Na-Ion Batteries. *Angew. Chem., Int. Ed.* **2024**, *63* (7), No. e202315371.
(41) McColl, K.; Coles, S. W.; Zarabadi-Poor, P.; Morgan, B. J.; Islam, M. S. Phase Segregation and Nanoconfined Fluid O_2 in a Lithium-Rich Oxide Cathode. *Nat. Mater.* **2024**, *23*, 826.